ADVANCED FUNCTIONAL MATERIALS
www.afm-journal.de

Anisotropic Growth of Nonlayered CdS on MoS_2 Monolayer for Functional Vertical Heterostructures

*Wei Zheng, Wei Feng, Xin Zhang, Xiaoshuang Chen, Guangbo Liu, Yunfeng Qiu, Tawfique Hasan, Pingheng Tan, and Ping An Hu**

2D semiconductors have emerged as a crucial material for use in next-generation optotelectronics. Similar to microelectronic devices, 2D vertical heterostructures will most likely be the elemental components for future nanoscale electronics and optotelectronics. To date, the components of mostly reported 2D van der Waals heterostructures are restricted to layer crystals. In this work, it is demonstrated that nonlayered semiconductors of CdS can be epitaxially grown on to 2D layered MoS_2 substrate to form a new quasi vertical heterostructure with clean interface by chemical vapor deposition. Photodetectors based on this CdS/MoS_2 heterostructure show broader wavelength response and ≈50-fold improvement in photoresponsivity, compared to the devices fabricated from MoS_2 monolayer only. This research opens up a way to fabricate a variety of functional quasi heterostructures from nonlayered semiconductors.

1. Introduction

Semiconductor heterostructures play a crucial role in modern microelectronics and optoelectronics.[1] Heterostructures, combining different materials, show bandgap offset and tunable electrical and optoelectrical properties. Conventional heterostructures are primarily based on group IV, III-V, or II-VI semiconductors, with covalent bonding between atoms at the hetero-interface.[1,2] The usage of material components for conventional heterostructures is strongly dictated by lattice mismatch which determines the interface quality and thus, the heterostructure performance. Beyond the traditional group IV, III-V, or II-VI semiconductors, 2D layered crystals (e.g., graphene,[3] transition metal dichalcogenides,[4] hexagonal boron nitride (*h*-BN),[5] phosphorene,[6] etc.) have emerged as promising candidates for next generation electronics and optoelectronics due to their unique properties. These 2D layered materials can be artificially combined to fabricate various van der Waals (vdW) heterostructures without the lattice match limitation. Novel physical properties of these vdW heterostructures have been investigated theoretically and experimentally, and devices based on those new heterostructures such as tunnel transistors and sensors have already been demonstrated.[7–11]

This far, these vdW heterostructures have mainly been fabricated by a top-down process of manual transfer or a bottom-up method of chemical vapor deposition (CVD) growth. The first demonstration of vdW heterostructures were realized by vertically stacking different 2D materials (graphene/*h*-BN,[8,12] MoS_2/graphene,[10] graphene/WS_2,[9] etc.) using conventional polymethyl-methacrylate-mediated transfer method.[7] The physical properties of these heterostructures are significantly influenced by relative orientation of the layers and interfacial quality between them. However, the stacking style and crystal orientation cannot be easily controlled by mechanical transfer method. In addition, such strategies cannot ensure good interfacial quality. Compared to manual transfer, CVD epitaxial growth is a powerful approach for fabricating 2D vdW heterostructures with controlled stacking style, crystal orientation, and clean interface. Indeed, using this strategy, some vertical heterostructures have already been successfully grown, including graphene/*h*-BN,[13] MoS_2/*h*-BN,[14] $MoSe_2$/graphene,[15] MoS_2/graphene,[16] WS_2/MoS_2,[17] and MoS_2/SnS_2.[18]

This far, the components of the reported 2D-vertical vdW heterostructures have been restricted to layered materials with planar crystal structures. However, many non-layered materials such as cadmium sulfide (CdS) also exhibit attractive optoelectronic properties.[19] Combination of such non-layered functional semiconductors with layered materials (e.g., MoS_2) could create a new type of vdW heterostructure to provide novel

W. Zheng, W. Feng, X. Chen, G. Liu, Dr. Y. Qiu, Prof. P. A. Hu
Key Laboratory of Micro-systems and Micro-structures Manufacturing of Ministry of Education
Harbin Institute of Technology
Harbin 150080, P. R. China
E-mail: hupa@hit.edu.cn

W. Zheng, W. Feng, Prof. P. A. Hu
School of Materials Science and Engineering
Harbin Institute of Technology
Harbin 150080, P. R. China

X. Zhang, Prof. P. H. Tan
State Key Laboratory of Superlattices and Microstructures
Institute of Semiconductors
Chinese Academy of Sciences
Beijing 100083, P. R. China

Dr. T. Hasan
Cambridge Graphene Centre
University of Cambridge
Cambridge CB3 0FA, UK

DOI: 10.1002/adfm.201504775

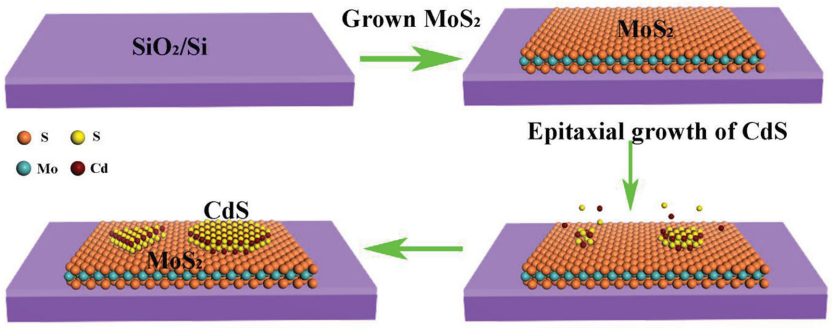

Figure 1. Schematic illustration of one-step epitaxial growth of CdS/MoS_2 heterostructures.

platform for applications in nanoscale electronics and optoelectronics. These non-layered materials typically incline to stack into 3D nanostructures due to their chain-like structure and the lack of driving force for 2D anisotropic growth. We note that some non-layered materials such as noble metals, metal oxides, and metal chalcogenides can be confined to 2D anisotropic growth to form sheet-like nanomaterials through the assistance of organic surfactants via wet chemical synthesis.[20] However, these soluble sheet-like ultrathin nanomaterials cannot be used for device applications as they become easily folded, crumpled, or aggregated when they are transferred onto substrates during device fabrication. In addition, these surface-ligand protected nanosheets are not suitable for the fabrication of clean interfaces. To realize these novel vdW heterostructures with high quality interface, direct anisotropic growth of non-layered semiconductors on layered 2D materials through a CVD process is the most realistic approach. However, such a process is yet to be demonstrated.

In this work, epitaxial growth of non-layered CdS nanosheet on ultrathin MoS_2 is demonstrated, thereby creating a new vdW vertical heterostructure. It is found that anisotropic growth of CdS on MoS_2 is driven by kinetics within a certain reaction temperature range influenced by the substrates, without forming energetically favored 3D structures. Photodetectors based on this CdS/MoS_2 heterostructure show broader wavelength response and significantly improved photoresponsivity compared to the devices fabricated from monolayer MoS_2 only.

2. Results and Discussion

Figure 1 shows the schematic representation of epitaxial growth of 2D CdS/MoS_2 vertical heterostructures (further information in Figure S1, Supporting Information). In the first stage, the left zone and MoO_3 zone in the furnace are heated to 250 and 670 °C, respectively. Subsequently, sulfur is pushed into the left zone quickly and kept for 25–30 min. This stage is used to grow MoS_2. In the second stage, the zone of substrate containing as-grown MoS_2 cools down to 500–600 °C, meanwhile CdS zone is heated to 950 °C. Finally the CdS stream is submitted using Ar gas to the surface of MoS_2 to form the vertical heterostructure.

The as-grown triangular MoS_2 nanoflakes with sizes of up to 30 µm lateral dimension are uniformly distributed over the substrate. Such a typical MoS_2 flake is shown in **Figure 2**a. Figure 2b shows a scanning electron microscope (SEM) image of the vertical heterostructures, in which the dark part of the image represents a MoS_2 nanocrystal and the bright triangles or hexagons are epitaxial CdS nanosheets. The CdS/MoS_2 heterostructures are further characterized using atomic force microscopy (AFM), (Figure 2c,d and Figure S2, Supporting Information). The thickness of the eptaxial CdS on MoS_2 is in the range of 10–60 nm. Figure 2c shows an AFM image of a hexagonal CdS crystal, with ≈50 nm uniform thickness. In Figure 2d, MoS_2 and CdS nanosheets with corresponding thicknesses of 1 and 30 nm can be observed on SiO_2/Si. Since CdS has two different crystal structures,[21] it is necessary to determine their crystallographic phase using X-ray diffraction (XRD). In Figure 2e, the dark gray plot represents the

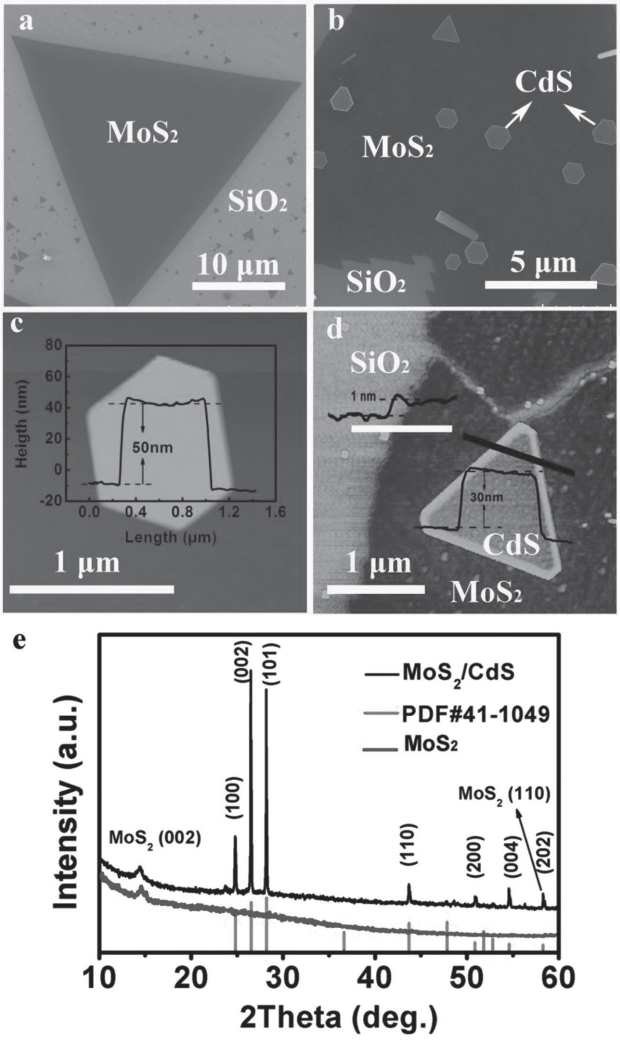

Figure 2. Characterization of vdW epitaxial CdS/MoS_2. a,b) SEM images of CVD grown triangle MoS_2 and CdS/MoS_2 heterostructures, respectively. c) AFM image and associated height profile of a hexagonal CdS. d) AFM phase image of the heterostructure with associated height profiles. e) XRD characterization of from top to bottom MoS_2/CdS, MoS_2, and PDF#41-1049.

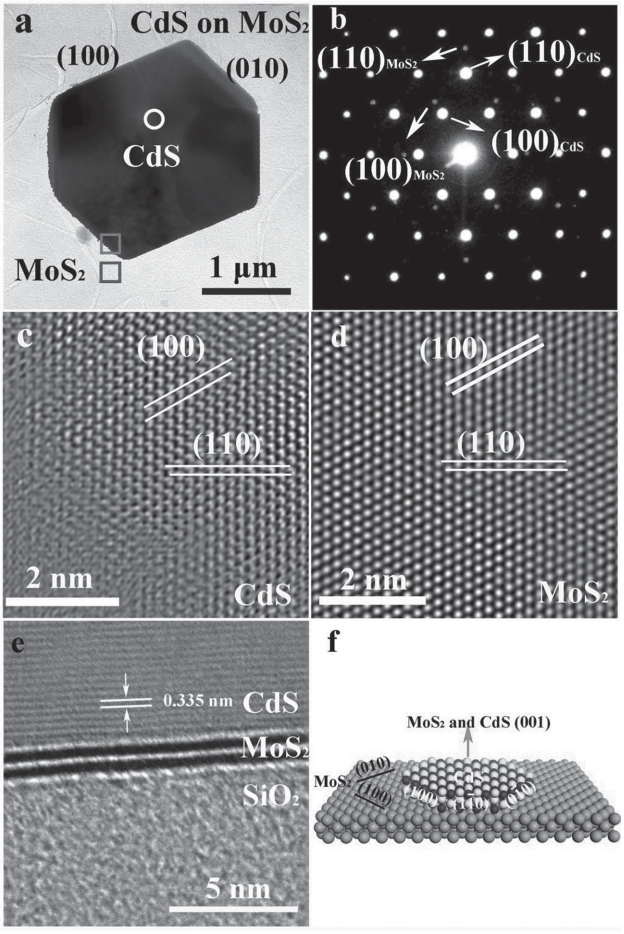

Figure 3. TEM characterization of the heterostructures. a) Low-magnification TEM images of CdS/MoS_2 heterostructures. b) Selected area electron diffraction (SAED) of heterostructures. c,d) Fast Fourier transform images of CdS and MoS_2, respectively. e) Cross-sectional TEM images of the CdS/MoS_2 heterostructure. f) Schematic model of the CdS/MoS_2 heterostructures.

XRD result of MoS_2, the light gray plot shows the CdS powder XRD patterns from the database (PDF#41-1049), while the black plot is that of the CdS/MoS_2 heterostructure. The diffraction pattern of the heterostructure can be perfectly indexed on the datebase of a hexagonally phased CdS and MoS_2.

To explore the effects of MoS_2 on the growth of CdS, the CdS/MoS_2 heterostructure is studied by transmission electron microscopy (TEM) (shown in **Figure 3**a and Figure S3, Supporting Information). Under TEM observation, the CdS sheets exhibit a deeper color while the MoS_2 films are almost transparent. A typical selected area electron diffraction (SAED) pattern (Figure 3b) is taken from the area of CdS/MoS_2 heterostructure (circle in Figure 3a). In this SAED pattern, two sets of six-fold symmetric diffraction spots are observed, in which the brighter and inner spots correspond to CdS (a = 4.14 Å) while the weaker set belongs to MoS_2 (a = 3.14 Å). By correlating the SAED pattern with the morphology (Figure 3a), the planes of the hexagonal CdS can be identified (Figure 3a), indicating that every plane of CdS is parallel to the corresponding MoS_2 plane, e.g., CdS (100) || MoS_2 (100) and CdS (110) || MoS_2 (110). Figure 3c,d shows the Fourier transform high-resolution TEM of CdS and MoS_2 which were measured from the red and blue squares in Figure 3a, respectively. Both CdS and MoS_2 exhibit high quality crystallinity. The results indicate that the spacings of (100) and (110) planes of CdS are 0.36 and 0.21 nm, while the planes of MoS_2 are 0.27 and 0.16 nm, respectively. These TEM characterization further demonstrate the good epitaxy of CdS on MoS_2 without any misorientation. Lattice mismatch between hexagonal CdS and MoS_2 is calculated to be 32% using the relationship $f = [d_{Cds}(100)\text{-}d_{MoS2}(100)]/d_{MoS2}(100)$,[22] where $d_{Cds}(100)$ = 0.359 nm, $d_{MoS2}(100)$ = 0.272 nm. This lattice mismatch is larger compared to the traditional group IV, III-V, or II-VI semiconductor heterostructures.[23] vdW epitaxy allows formation of high quality heterostructure consisting of two crystals with such large lattice mismatch because of the weak vdW interaction at the interface. We note that this is also applicable to manually stacked crystals. The cross-sectional electron microscope images with clean interfaces without significant interlayer atomic mixing is shown in Figure 3e, guaranteeing the heteroepitaxial stacking. In addition, as shown in the SEM image in Figure S4 (Supporting Information), the CdS nanosheets show parallel edges, as indicated by the blue and red lines. This crystal orientation alignment (CdS (100) || MoS_2 (100) and CdS (110) || MoS_2 (110)) is attributed to vdW epitaxy. Based on the above discussion, we present a scheme of epitaxially grown CdS on MoS_2 in Figure 3f. This shows that hexagonal CdS is grown parrallel to the (001) plane surface of MoS_2 in the six equivalent directions (such as 110), rather than the preferential (001) direction. It is proposed that this growth kinetics is induced by the MoS_2 substrate.

To further investigate our proposal on the anisotropic growth of CdS by substrate induced kinetics, a controlled experiment is performed on the growth of CdS nanocrystals on SiO_2/Si under identical reaction parameters. This produces rod-like CdS nanocrystals, clearly showing an energetically favorable growth direction of (001) the hexagonal crystals (Figure S5, Supporting Information). This substrate-dependent growth can be well-understood by its surface energy E_s or its attachment energy E_a. A smaller value of E_s ensures higher stability while a larger $|E_a|$ indicates a faster growth process. The value of E_s and $|E_a|$ of $(001)_{CdS}$, calculated by ref. [21] are much higher than any other CdS plane. This indicates that the surface of $(001)_{CdS}$ is more active, with much faster growth rate than any other face under normal condition. This is why compared to the growth of CdS on MoS_2 (Figure 2b), CdS tripod nanocrystal is predominantly grown on SiO_2/Si (Figure S5a, Supporting Information). Indeed, the growth rate of the legs along the (001) crystallographic orientation on SiO_2/Si is much higher than that along the other surfaces (the model of tripod nanocrystal is shown in Figure S6, Supporting Information). On the other hand, the shapes grown on MoS_2 are different due to the substrate lattice structure and the energy barrier for nucleation (ΔG^*) at the growth temperature. Reference [24] has recently discussed growth kinetics on layered crystals that explains our observation. According to classical nucleation kinetics, the free energy change for nucleation at heterostructures can be written as follows: $\Delta G_{r,\gamma} = \pi r^2 t \Delta G_v + \pi r^2(\gamma_c + \gamma_{sc} - \gamma_s) + 2\pi r t \gamma_{c,edge}$.[24] Here r and t are radius and thickness of nucleus

of CdS. γ_s, γ_c, γ_{sc}, and $\gamma_{c,edge}$ represent the E_s of the substrate (MoS_2 or SiO_2 in our case), E_s of the nucleus of the CdS crystals, interfacial energy between the nucleus and the substrate and the E_s of nucleus edge of CdS crystals, respectively. The difference in free energy per unit volume during nucleation is expressed as ΔG_v. The maximum point $\Delta G_{r,\gamma}$ in the total Gibbs free energy corresponds to the critical free energy barrier for nucleation $\Delta G^* = \pi r(\gamma_{c,edge})^2/[\Delta G_v - (\gamma_c + \gamma_{sc} - \gamma_s)/t]$.[24] The term $(\gamma_c + \gamma_{sc} - \gamma_s)$ represents the effective change in E_s during the nucleation and is largely dependent on the growth substrate. The surface energy of MoS_2 is ≈70–75 mJ m^{-2}.[25] On the other hand, CdS grown on SiO_2 forms tripod structures due to the significantly larger E_s of the substrate (γ_{SiO2} ≈ 300–400 mJ m^{-2}).[26] This indicates that a larger free energy barrier must be overcome for CdS growth on SiO_2/Si compared to the epitaxial growth of CdS on MoS_2 surface. It is also noted that the CdS growth is further impacted by the reaction temperature. Above 1000 °C, CdS nanocrystals always grow in energically favorable (001) direction on both the SiO_2 and MoS_2 substrates, forming rod-like nanocrystals (Figure S5b, Supporting Information). This is mainly attributed to the high concentration of precursor and the enhanced activity of CdS is at such high temperature (>1000 °C). Since the growth rate increases faster along the (001) plane compared to that of the (100) plane under high temperature, the CdS nanocrystals tend to develop a rod-like morphology. Therefore, tripod-like structures (Figure S5b, Supporting Information) rather than nanosheets (Figure 2b) of CdS nanocrystals are observed on MoS_2 surface for high temperature growth.

Raman and photoluminescence (PL) are effective ways to characterize the crystal quality and band gap of these materials. The CdS/MoS_2 heterostructures (hexagonal CdS on MoS_2 in **Figure 4**a and triangular CdS on MoS_2 in Figure S7, Supporting Information) are characterized by Raman and PL with a 488 nm

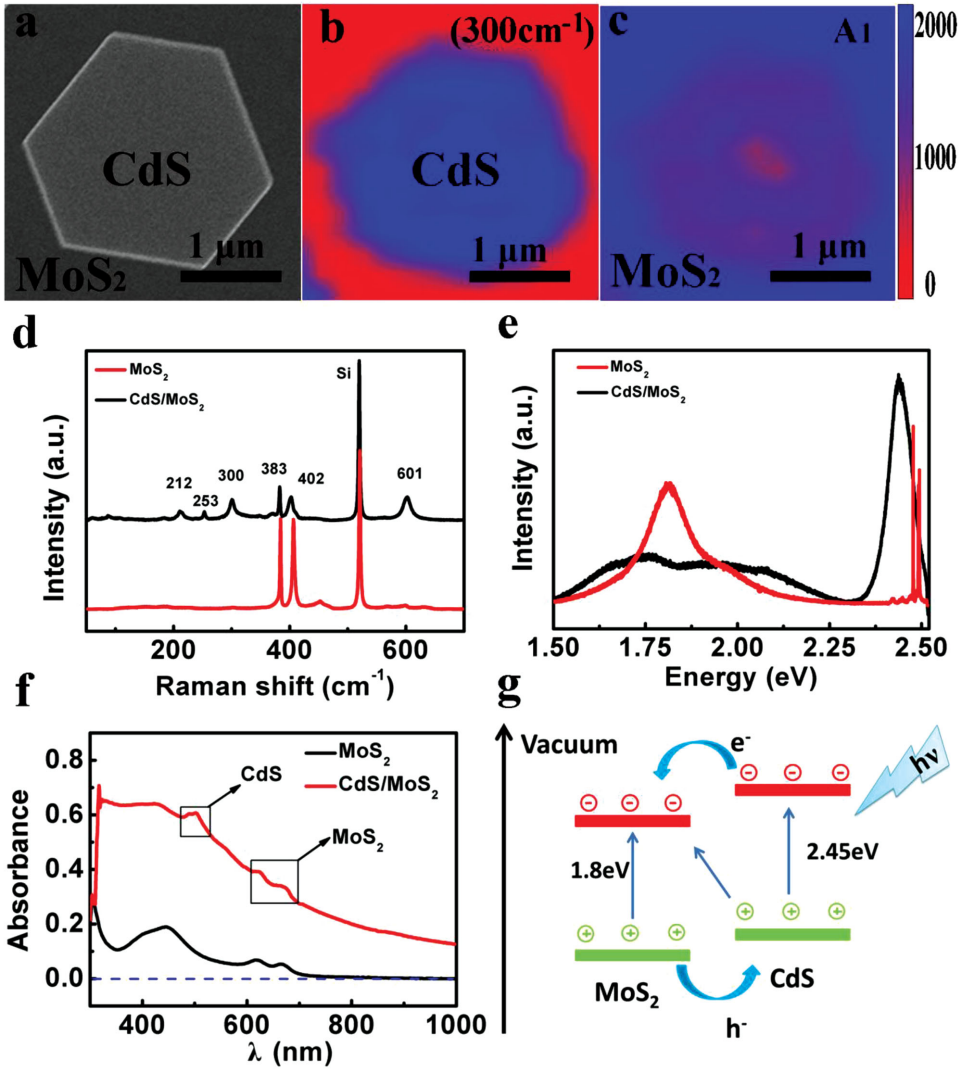

Figure 4. Spectroscopic characterizations of the as-grown CdS/MoS_2 heterostructures. a) SEM image of hexagonal CdS on MoS_2. b) Raman mapping of CdS at 300 cm^{-1}. c) Raman mapping of MoS_2 at 402.1 cm^{-1}. d,e) Raman and PL spectra of the CdS/MoS_2 heterostructures. f) UV–vis–NIR spectra of the CdS/MoS_2 heterostructures and single-layer MoS_2. g) Band gap schematic of CdS/MoS_2 heterostructure photodetector under illumination.

laser. The Raman mapping of CdS 1LO mode at 300 cm^{-1} is shown in Figure 4b. The blue hexagon in the center is the CdS hexagon while the red zone represents MoS_2. Figure 4c shows the Raman mapping at A_{1g} mode of MoS_2. Raman signal of MoS_2 can be obtained from the entire area of the sample. However, the Raman signal of the central area where CdS is grown is much weaker. This Raman mapping further demonstrates the epitaxial nature of the structure. The Raman spectra of the heterostructures are shown in Figure 4d. The peaks of E_{2g} mode at 383 cm^{-1} and A_{1g} mode at 402 cm^{-1} are the characteristic peaks of MoS_2. On the other hand, the peaks at 212, 254, 300, and 601 cm^{-1} are the characteristic peaks of CdS.[19] The PL spectra of the heterostructures are shown in Figure 4e. We identified PL peak of MoS_2 at 1.81 eV. However, this peak disappeared after the formation of CdS/MoS_2 heterostructure, accompanied by the appearance of a new peak at ≈1.70 eV (Details on PL measurements using a 532 nm laser is presented in Figure S8, Supporting Information). The peak at 1.70 eV can be attributed to the interlayer excitonic transition of MoS_2 conduction band maxima to the CdS valence band minima.[17] The three peaks in red line at 2.477, 2.491, and 2.493 eV indicate the Raman peaks of Si, A_{1g} mode and E_{2g} mode of MoS_2, respectively. The peak at 2.45 eV indicates the existence of CdS. Because CdS has a strong visible optical absorption, it is an attractive material for enhancement of light absorption and photoresponse of the heterostructure. UV–vis–NIR absorption spectra of MoS_2 and CdS/MoS_2 heterostructures are measured by transferring 0.5 cm × 0.5 cm MoS_2 and CdS/MoS_2 films on to glass substrates; Figure 4f. The coverage of CdS on MoS_2 is ≈20%, estimated from a series of SEM images. The plots indicate that the single layer MoS_2 has a weak light absorption and a small response scope (wavelength < 680 nm). Compared to MoS_2, the CdS/MoS_2 heterostructures have a much higher absorption and wider light response (wavelength < 1000 nm). The higher absorption and stronger response can be explained by the band structure of the heterostructure; Figure 4g.[27] Due to lower conduction band edge of MoS_2, electrons located in the conduction band of CdS tend to transfer to the conduction band of MoS_2, which leads to effective separation of electron–hole pairs and prevents the electron–hole recombination. Therefore, the number of carriers increases in the circuit, leading to the enhancement of photocurrent. It is noted that the broadening of response wavelength of the heterostructure is expected to reach to up to 730 nm after the formation of the vertical heterostructure. However, the UV–vis–NIR spectra of the CdS/MoS_2 heterostructures indicates absorbance above 730 nm. This is likely due to the variation in shape, size and thickness of the CdS nanoscrytals.

The single-layer MoS_2 and CdS/MoS_2 heterostructure-based photodetectors are fabricated using Ti/Au contacts on silicon substrates covered with 300 nm silicon oxide (SiO_2/Si). **Figure 5**a presents a schematic diagram of a single-layer MoS_2 photodetector with epitaxially grown CdS. The inset shows an optical microscope image of the actual device. The photoelectrical characterizations are measured at room temperature in ambient condition. As shown in Figure 5b, the photocurrent as a function of time is measured under alternative dark and illumination condition at 0.266 mW cm^{-2}, with a bias

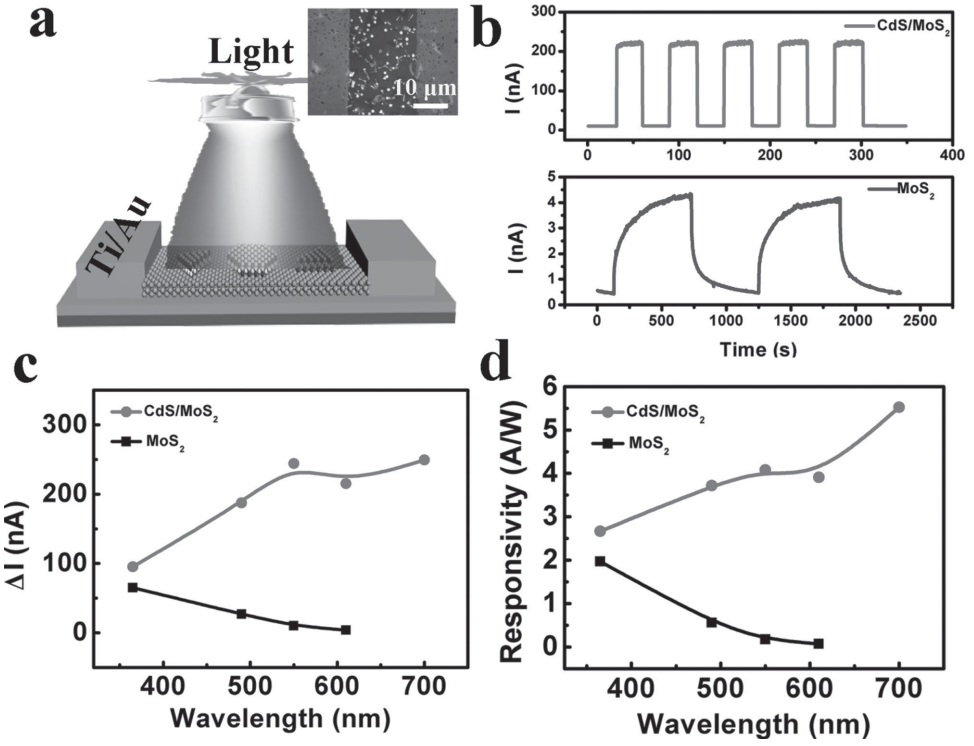

Figure 5. Characterizations of the photodetectors. a) Schematic of CdS/MoS_2 heterostructure photodetector; inset shows an optical microscope image of the device. b) Time-dependent photoresponse of CdS/MoS_2 heterostructure and single-layer MoS_2 photodetectors under 610 nm illumination, with a 1 V bias. c,d) Photocurrent and photoresponsivity under 365, 490, 550, 610, and 700 nm wavelength of the same devices.

voltage V_{ds} = 1 V and a gate voltage V_g = 0 V. At 610 nm (other wavelengths are shown in the Supporting Information) ON and OFF illumination, both the single-layer MoS_2 and CdS/MoS_2 heterostructure-based photodetectors exhibit repeatable and stable response to the light. The response (light ON) and recovery (light OFF) time is calculated by averaging the device response and considering the time it takes to reach 80% of the final values. The measured rise time is 100 ms, much faster than that of the devices based on CVD grown single-layer MoS_2 (rise time > 10 s). Compared to the MoS_2 photodetector, the CdS/MoS_2 devices exhibit strong photocurrent enhancement under this illumination. Here, photocurrent (ΔI) is defined as the difference between I_{ON} and I_{OFF} with a voltage bias of 1 V. Figure 5c shows the photocurrents of the MoS_2 and CdS/MoS_2 photodetectors under light with a series of wavelengths (365, 490, 550, 610, and 700 nm). The photocurrent from MoS_2-based device gradually drops with the increase in wavelength, while that of the CdS/MoS_2-based device rises fast and reaches the maximum at 700 nm. Note that there is no significant response to light when the illumination wavelength is longer than the optical band gap of the single layer MoS_2 (1.82 eV, λ = 681 nm). This is because only the incident photons with energies exceeding 1.82 eV excite electrons from the valence band into the conduction band of MoS_2. CdS has a band gap of 2.45 eV. Thus the CdS photodetector is not expected respond to >506 nm. However, we observe photoresponse of the CdS/MoS_2 detector at >680 nm. We propose that the photoresponse in this forbidden optical absorption region for pristine MoS_2 arises from the photoinduced electron transfer from the valence band of CdS to the bottom of conduction band of MoS_2.

Responsivity (R_λ) is another critical parameter to evaluate the performance of a photodetector. R_λ is defined as the photocurrent generated per unit power of the incident light on the effective device area. The value of R_λ can be calculated using the relation: $R_\lambda = \Delta I / P_\lambda S$. Here, ΔI is the generated photocurrent, P_λ is the incident light intensity, S is the effective illuminated area (In the present study $S \approx 1$ mm × 20 μm). The photoresponsivity under different wavelengths of MoS_2 and CdS/MoS_2 photodetectors is measured and the results are shown in Figure 5d. The results demonstrate that the epitaxial CdS plays an important role to enhance the photoresponsivity, with over 50 times increase in responsivity (70.8 mA W^{-1} vs 3.91 A W^{-1}) under 610 nm illumination. Such a strong enhancement in photoresponsivity and simple device configuration underscores the potential application of this CdS/MoS_2 heterostructure.

3. Conclusions

In summary, epitaxial growth of nonlayered CdS onto MoS_2 was achieved using a one-step CVD method, resulting in vertical heterostructures. It is proposed that the substrate surface energy plays an important role in the growth of CdS. Furthermore, the feasability of CdS/MoS_2 heterostructure-based photodetectors is demonstrated. The photocurrent and photoresponsivity of CdS/MoS_2 heterostructure-based photodetectors are greatly enhanced, compared to their MoS_2 counterparts, making the presented strategy very attractive for high-performance optelectronic devices.

4. Experimental Section

Characterizations: The as-grown CdS/MoS_2 heterostructures were characterized by SEM (Hitachi S-4200), AFM (Nanoscope IIIa Vecco), UV–vis–NIR absorption (Hitachi U-4100), TEM (Tacnai-G2 F30, accelerating voltage of 300 kV), and Raman spectroscopy (LabRAM XploRA, power of 0.15 mW, excitation wavelength of 488 and 532 nm). The detectors were annealed at 200 °C for 30 min with 100 sccm Ar : H_2 (V/V = 9/1) to reduce the resistance and improve the contact for the devices.

Electrical Measurements: These devices were characterized using a semiconductor analyzer (Keithley 4200 SCS) combined with a Lakeshore probe station. Photoelectric data were obtained by using a 500 W xenon lamp as the light source. Monochromatic lights of 254–850 nm were obtained using optical filters. The intensities of the incident light source were measured by a power and energy meter (Model 372, Scienteck). The photocurrent measurements were performed using the Lakeshore probe station and an HP 4140B Semiconductor Parameter Analyzer.

Supporting Information

Supporting Information is available from the Wiley Online Library or from the author.

Acknowledgements

This work was supported by the National Natural Science Foundation of China (NSFC, Nos.61390502, 21373068,11225421,11474277,11434010), the National key Basic Research Program of China (973 Program) under Grant No. 2013CB632900. T.H. acknowledges support from a Royal Academy of Engineering Research Fellowship (Graphlex).

Received: November 7, 2015
Revised: January 3, 2016
Published online: February 10, 2016

[1] Y. Ohno, D. K. Young, B. Beschoten, F. Matsukura, H. Ohno, D. D. Awschalom, *Nature* **1999**, *402*, 790.
[2] R. Gaska, J. W. Yang, A. Osinsky, Q. Chen, M. A. Khan, A. O. Orlov, G. L. Snider, M. S. Shur, *Appl. Phys. Lett.* **1998**, *72*, 707.
[3] K. S. Novoselov, A. K. Geim, S. V. Morozov, D. Jiang, Y. Zhang, S. V. Dubonos, I. V. Grigorieva, A. A. Firsov, *Science* **2004**, *306*, 666.
[4] a) S. Z. Butler, S. M. Hollen, L. Cao, Y. Cui, J. A. Gupta, H. R. Gutiérrez, T. F. Heinz, S. S. Hong, J. Huang, A. F. Ismach, E. Johnston-Halperin, M. Kuno, V. V. Plashnitsa, R. D. Robinson, R. S. Ruoff, S. Salahuddin, J. Shan, L. Shi, M. G. Spencer, M. Terrones, W. Windl, J. E. Goldberger, *ACS Nano* **2013**, *7*, 2898; b) Q. H. Wang, K. Kalantar-Zadeh, A. Kis, J. N. Coleman, M. S. Strano, *Nat. Nanotechnol.* **2012**, *7*, 699; c) M. Chhowalla, H. S. Shin, G. Eda, L. J. Li, K. P. Loh, H. Zhang, *Nat. Chem.* **2013**, *5*, 263.
[5] K. K. Kim, A. Hsu, X. Jia, S. M. Kim, Y. Shi, M. Dresselhaus, T. Palacios, J. Kong, *ACS Nano* **2012**, *6*, 8583.
[6] H. Liu, A. T. Neal, Z. Zhu, Z. Luo, X. Xu, D. Tománek, P. D. Ye, *ACS Nano* **2014**, *8*, 4033.
[7] A. K. Geim, I. V. Grigorieva, *Nature* **2013**, *499*, 419.
[8] L. Britnell, R. V. Gorbachev, R. Jalil, B. D. Belle, F. Schedin, A. Mishchenko, T. Georgiou, M. I. Katsnelson, L. Eaves, S. V. Morozov, N. M. R. Peres, J. Leist, A. K. Geim, K. S. Novoselov, L. A. Ponomarenko, *Science* **2012**, *335*, 947.
[9] T. Georgiou, R. Jalil, B. D. Belle, L. Britnell, R. V. Gorbachev, S. V. Morozov, Y.-J. Kim, A. Gholinia, S. J. Haigh, O. Makarovsky,

L. Eaves, L. A. Ponomarenko, A. K. Geim, K. S. Novoselov, A. Mishchenko, *Nat. Nanotechnol.* **2013**, *8*, 100.
[10] W. J. Yu, Y. Liu, H. Zhou, A. Yin, Z. Li, Y. Huang, X. Duan, *Nat. Nanotechnol.* **2013**, *8*, 952.
[11] R. Cheng, D. Li, H. Zhou, C. Wang, A. Yin, S. Jiang, Y. Liu, Y. Chen, Y. Huang, X. Duan, *Nano Lett.* **2014**, *14*, 5590.
[12] W. Gannett, W. Regan, K. Watanabe, T. Taniguchi, M. F. Crommie, A. Zettl, *Appl. Phys. Lett.* **2011**, *98*, 242105.
[13] Z. Liu, L. Song, S. Zhao, J. Huang, L. Ma, J. Zhang, J. Lou, P. M. Ajayan, *Nano Lett.* **2011**, *11*, 2032.
[14] X. Ling, Y.-H. Lee, Y. Lin, W. Fang, L. Yu, M. S. Dresselhaus, J. Kong, *Nano Lett.* **2014**, *14*, 464.
[15] G. W. Shim, K. Yoo, S.-B. Seo, J. Shin, D. Y. Jung, I.-S. Kang, C. W. Ahn, B. J. Cho, S.-Y. Choi, *ACS Nano* **2014**, *8*, 6655.
[16] Y. M. Shi, W. Zhou, A. Y. Lu, W. J. Fang, Y. H. Lee, A. L. Hsu, S. M. Kim, K. K. Kim, H. Y. Yang, L. J. Li, J. C. Idrobo, J. Kong, *Nano Lett.* **2012**, *12*, 2784.
[17] Y. Gong, J. Lin, X. Wang, G. Shi, S. Lei, Z. Lin, X. Zou, G. Ye, R. Vajtai, B. I. Yakobson, H. Terrones, M. Terrones, B. K. Tay, J. Lou, S. T. Pantelides, Z. Liu, W. Zhou, P. M. Ajayan, *Nat. Mater.* **2014**, *13*, 1135.
[18] X. Zhang, F. Meng, J. R. Christianson, C. Arroyo-Torres, M. A. Lukowski, D. Liang, J. R. Schmidt, S. Jin, *Nano Lett.* **2014**, *14*, 3047.
[19] a) Q. H. Li, T. Gao, T. H. Wang, *Appl. Phys. Lett.* **2005**, *86*, 193109; b) Y.-F. Lin, J. Song, Y. Ding, S.-Y. Lu, Z. L. Wang, *Adv. Mater.* **2008**, *20*, 3127.
[20] a) C. Tan, H. Zhang, *J. Am. Chem. Soc.* **2015**, *137*, 12162; b) C. Tan, H. Zhang, *Chem. Soc. Rev.* **2015**, *44*, 2713.
[21] S. H. Shah, A. Azam, M. A. Rafiq, *Cryst. Growth Des.* **2015**, *15*, 1792.
[22] H. Zhou, F. Yu, C. F. Guo, Z. Wang, Y. Lan, G. Wang, Z. Fang, Y. Liu, S. Chen, L. Sun, Z. Ren, *Nanoscale* **2015**, *7*, 9153.
[23] a) J. Zhang, M. Brehm, M. Grydlik, O. G. Schmidt, *Chem. Soc. Rev.* **2015**, *44*, 26; b) G. Chuan Fei, W. Yongsheng, J. Peng, C. Sihai, M. Junjie, Z. Zhuwei, L. Qian, *Nanotechnology* **2008**, *19*, 445710; c) J. Liao, B. Sa, J. Zhou, R. Ahuja, Z. Sun, *J. Phys. Chem. C* **2014**, *118*, 17594.
[24] H. Heo, J. H. Sung, G. Jin, J.-H. Ahn, K. Kim, M.-J. Lee, S. Cha, H. Choi, M.-H. Jo, *Adv. Mater.* **2015**, *27*, 3803.
[25] J. N. Coleman, M. Lotya, A. O'Neill, S. D. Bergin, P. J. King, U. Khan, K. Young, A. Gaucher, S. De, R. J. Smith, I. V. Shvets, S. K. Arora, G. Stanton, H.-Y. Kim, K. Lee, G. T. Kim, G. S. Duesberg, T. Hallam, J. J. Boland, J. J. Wang, J. F. Donegan, J. C. Grunlan, G. Moriarty, A. Shmeliov, R. J. Nicholls, J. M. Perkins, E. M. Grieveson, K. Theuwissen, D. W. McComb, P. D. Nellist, V. Nicolosi, *Science* **2011**, *331*, 568.
[26] a) J. Mizele, J. L. Dandurand, J. Schott, *Surf. Sci.* **1985**, *162*, 830; b) R. Cabriolu, P. Ballone, *Phys. Rev. B* **2010**, *81*, 155432.
[27] a) S. H. Yu, Y. Lee, S. K. Jang, J. Kang, J. Jeon, C. Lee, J. Y. Lee, H. Kim, E. Hwang, S. Lee, J. H. Cho, *ACS Nano* **2014**, *8*, 8285; b) J. A. Herron, J. Kim, A. A. Upadhye, G. W. Huber, C. T. Maravelias, *Energy Environ. Sci.* **2015**, *8*, 126.